Front. Chem. Sci. Eng. 2023, 17(5): 504−515
https://doi.org/10.1007/s11705-022-2260-1

RESEARCH ARTICLE

Electrospun porous carbon nanofibers derived from bio-based phenolic resins as free-standing electrodes for high-performance supercapacitors

Yongsheng Zhang[1], Xiaomeng Yang[1], Jinpan Bao[1], Hang Qian[1], Dong Sui[2], Jianshe Wang[1], Chunbao Charles Xu (✉)[3], Yanfang Huang (✉)[1]

1 School of Chemical Engineering, Zhengzhou University, Zhengzhou 450001, China
2 School of Chemistry and Chemical Engineering, Luoyang Normal University, Luoyang 471934, China
3 Department of Chemical and Biochemical Engineering, Western University, London, N6A 3K7, Canada

Abstract Phenolic resins were employed to prepare electrospun porous carbon nanofibers with a high specific surface area as free-standing electrodes for high-performance supercapacitors. However, the sustainable development of conventional phenolic resin has been challenged by petroleum-based phenol and formaldehyde. Lignin with abundant phenolic hydroxyl groups is the main non-petroleum resource that can provide renewable aromatic compounds. Hence, lignin, phenol, and furfural were used to synthesize bio-based phenolic resins, and the activated carbon nanofibers were obtained by electrospinning and one-step carbonization activation. Fourier transform infrared and differential scanning calorimetry were used to characterize the structural and thermal properties. The results reveal that the apparent activation energy of the curing reaction is 89.21 $kJ \cdot mol^{-1}$ and the reaction order is 0.78. The activated carbon nanofibers show a uniform diameter, specific surface area up to 1100 $m^2 \cdot g^{-1}$, and total pore volume of 0.62 $cm^3 \cdot g^{-1}$. The electrode demonstrates a specific capacitance of 238 $F \cdot g^{-1}$ (0.1 $A \cdot g^{-1}$) and good rate capability. The symmetric supercapacitor yields a high energy density of 26.39 $W \cdot h \cdot kg^{-1}$ at 100 $W \cdot kg^{-1}$ and an excellent capacitance retention of 98% after 10000 cycles. These results confirm that the activated carbon nanofiber from bio-based phenolic resins can be applied as electrode material for high-performance supercapacitors.

Keywords lignin, bio-based phenolic resins, electrospinning, activated carbon nanofibers, supercapacitors

Received July 5, 2022; accepted September 13, 2022

E-mails: cxu6@uwo.ca (Xu C. C.), hlele114@163.com (Huang Y.)

1 Introduction

Supercapacitors have attracted widespread attention due to their excellent performance at high power density, fast charge–discharge rate, long cycle life, and safety [1–3]. Therefore, they have widely satisfied the requirements of the applications for vehicles, portable electronics, etc. [4]. Carbon materials, such as activated carbon [5], carbon nanotubes [6], graphene [7], carbon nanofibers (CNFs) [8], and carbide-derived carbons [9], are extensively used as electrodes to store the electric charges on the surface and internal pore structure of the electrode through reversible ion adsorption/desorption at the electrode/electrolyte interface [10]. The specific capacitance of supercapacitors is mainly related to the specific surface area (SSA) of electrode materials [11]. Therefore, CNFs have received substantial attention as promising candidates for efficient electrode materials due to their high conductivity, large SSA, and free-standing property [12]. Ma et al. [8] successfully prepared CNFs with an SSA of 416 $m^2 \cdot g^{-1}$ and a remarkable specific capacitance of 171 $F \cdot g^{-1}$ at a low scanning rate of 5 $mV \cdot s^{-1}$. This result suggests that CNFs can be used as effective electrode material for supercapacitors and other energy storage devices.

Electrospinning is a facile method to prepare three-dimensional networks of CNFs with diameters ranging from tens of nanometers to several micrometers. Phenolic resin has been widely used as a carbon precursor due to certain features, such as high carbon yield, good thermal stability, good spinnability, and low cost [13]. However, the sustainable development of phenolic resin demands alternatives to feedstocks from expensive and non-renewable fossil resources. The World Health

Organization's International Agency for Research has classified formaldehyde as a carcinogen with genotoxicity [14]. Therefore, the development and utilization of green, healthy and bio-renewable precursor materials to synthesize phenolated depolymerized-lignin furfural resin (PDLF) is an optimal strategy. According to previously reported, lignin shows great potential for the preparation of value-added materials because of its low cost, eco-friendliness, high carbon contents, and unique aromatic structure [15]. Cheng et al. [16] successfully synthesized phenolic resins using aromatic and phenolic chemicals from alkali lignin depolymerization to replace petroleum-based phenol. Although there have been studies on the use of CNFs as electrode material for supercapacitors, to date, very few studies have examined the preparation of CNFs using bio-based phenolic resin synthesized from lignin and furfural as electrode material for supercapacitors.

In this work, aromatic and phenolic chemicals were obtained from lignin partially replacing phenol and furfural substituting formaldehyde in the synthesis of PDLF resin. Free-standing activated carbon nanofibers (ACNF-PDLF) with a high SSA were obtained by electrospinning combined with one-step carbonization activation. The mixture of KCl and $ZnCl_2$ as an activator avoids equipment corrosion and can be recycled. The structure, thermal properties, and porosity of ACNF-PDLF were characterized, as well as their electrochemical properties as electrodes for supercapacitors were tested. ACNF-PDLF with a novel micro/mesoporous structure and excellent electrochemical performance has great potential for application in electrochemical and advanced materials.

2 Experimental

2.1 Materials

Alkali lignin was supplied by Duly Reagent Co. Ltd., Nanjing, China. Analytical grade solvents and chemicals were purchased from Aladdin Reagent Co. Ltd., Shanghai, China, including ethanol, methanol, phenol, formaldehyde (37 wt %), tetrahydrofuran (containing 250 ppm butylated hydroxytoluene), furfural (99%), potassium carbonate (99%), sodium hydroxide (96%), potassium hydroxide (90%), polyvinyl butyral (PVB, M_w = 40000–70000), and epoxy resins.

2.2 Synthesis of PDLF resin

Briefly, to obtain low molecular weight lignin, 20 g lignin and 200 mL water−ethanol co-solvent (50/50 by volume) were added to an autoclave and catalyzed by NaOH. Then, the autoclave was purged with N_2 for 1 min to remove the air completely. Lignin was depolymerized under N_2 (270 °C for 2 h, 100 r·min^{-1}) from the pre-set pressure 1.5 MPa. The degraded mixture was filtered with filter paper and the solid residue was rinsed with ethanol. The filtrate was neutralized with 1 mol·L^{-1} HCl and the solvents were removed with a rotary evaporator under reduced pressure at 55 °C to obtain depolymerized-lignin (DL).

Then 14 g DL, 14 g phenol, and 0.8 g NaOH, were mixed into a three-neck flask. The DL was phenolated with stirring for 1.5 h at 90 °C. The mixture was adjusted with 1 mol·L^{-1} HCl until pH 7 and dried at 55 °C to obtain phenolated depolymerized-lignin (PDL).

PDLF resin was synthesized with PDL as the replacement for phenol. First, 13.54 g PDL and 0.85 g NaOH were mixed into a flask. The mixture was heated up to 70 °C and 11.63 g of furfural was added dropwise, and maintained at 70 °C for 1.5 h. Then the remaining furfural (4.98 g) was added at 120 °C and polymerized for 1.5 h. Finally, the PDLF resin was treated in vacuum oven at 55 °C for 5 h.

Conventional phenol formaldehyde resin (PF) was synthesized through a typical reaction; 11.2 g water, 28 mL ethanol, and 2.8 g NaOH were charged into a three-neck flask and stirred at 50 °C for 1 h. Then, 28 g phenol was added and kept at 80 °C for 2 h. The mixture was then cooled at 70 °C and 31.4 g formaldehyde was added and maintained at 80 °C for 2 h.

2.3 Preparation of CNF and ACNF

To obtain the spinning precursor of CNFs, 0.06 g PVB, 5 g PDLF, 0.5 g epoxy resin, and 4.44 g methanol were blended. PVB was used to improve the spinnability and viscosity of the spinning fluid.

The spinning fluid was inhaled into a 10 mL syringe and installed to the corresponding position of the electrostatic spinning machine (HD-2335, Beijing Yongkang Entertainment Industry Co. Ltd., China) under room temperature and humidity. The spinning potential difference between the electrodes was 14 kV, and the distance between the tip and the collector was 15 cm. The injected rate and needle horizontally moving rate were 1 mL·h^{-1} and 5 mm·s^{-1}, respectively.

Nanofibers (NF) were cured under ramping temperature profiles of 100, 130, 150, and, 180 °C for 1 h. Afterward, NF was carbonized at 800 °C in a tube furnace for 2 h under N_2 atmosphere. To further enhance the porosity, NF was immersed in a mixed solution of potassium chloride and zinc chloride (KCl:$ZnCl_2$ = 1:1 by mol) for 2 h, then filtered and dried at 60 °C. ACNF was gained at 800 °C in furnace for 2 h in an N_2 atmosphere. ACNF from traditional phenol formaldehyde resin were obtained accordingly.

2.4 Characterization

Fourier transform infrared (FTIR, PerkinElmer, USA)

spectra of samples were obtained using the potassium bromide tablet method at wavenumbers of 400–4000 cm^{-1}. The chemical structure of PDL and PDLF resin was analyzed on a 600 MHz ^1H nuclear magnetic resonance instrument (NMR, HD400MH, BrukerAvance, Germany) at room temperature. The molecular weight distribution profiles of PDLF resin were measured by gel permeation chromatography (GPC, CO-1000 RI at 40 °C, PL-gel 3 μm MIXED-E 300 × 7.5 mm column at 45 °C, Agilent, USA) using tetrahydrofuran as the eluent at 1 $mL \cdot min^{-1}$. Linear polystyrene of various molecular weights was employed as a standard for molecular weight calibration. The microstructure of the CNFs was characterized by scanning electron microscopy (SEM, SU 3500, Hitachi, Japan) and transition electron microscopy (TEM, JEM-2100F, JEOL, Japan). Raman analysis was performed on a LabRAM HR Evo from France. The conductivity data of fiber samples were obtained on a four-probe tester (ST2258C, Suzhou Lattice Electronics Co. Ltd., China). The surface elements of the carbon nanofibers were evaluated by an X-ray photoelectron spectrometer (XPS, ESCALAB 250Xi, ThermoFischer, USA). The thermal curing properties of the CNFs and curing kinetics of PDLF resin were evaluated with a thermogravimentry-differential scanning calorimetry (TG-DSC) system (DTG-60H, Shimadzu, Japan) under 50 $mL \cdot min^{-1}$ N_2 at different heating rate between 30 and 300 °C. N_2 adsorption/desorption isotherms were obtained at –196.15 °C using an ASAP 2020 physisorption analyzer (Micrometitics, USA).

2.5 Electrochemical measurements

CNFs or ACNF (1 cm × 1 cm, 2 mg) was pressed on nickel foam as the working electrode. The three-electrode test was carried out in 6 $mol \cdot L^{-1}$ KOH solution, using Pt plate and Hg/HgO as the counter electrode and reference electrode, respectively. Symmetric supercapacitors were prepared by using fiber samples with similar weights (Ø14 mm, 9 mg) as anode and cathode, polypropylene as separator (Ø16 mm), and 1 $mol \cdot L^{-1}$ Na_2SO_4 as electrolyte. The electrochemical performances were measured on electrochemical workstation (AUT86544, Metrohm Co. Ltd.) and a battery test system (Land CT2001A, Wuhan Jinnuo Electronic Co. Ltd.), including cyclic voltammetry (CV), electrochemical impedance spectroscopy (EIS, test frequency ranging from 0.01 to 100000 Hz), and galvanostatic charge–discharge (GCD). The voltage ranges in the two- and three-electrode test systems were 0–1 and –0.98–0 V, respectively.

For the three-electrode system, the mass ratio capacitance of the CNFs was calculated according to the GCD curves and the following equation:

$$C = \frac{I\Delta T}{m\Delta U}, \tag{1}$$

where C ($F \cdot g^{-1}$) is the mass ratio capacitance, I (A) is the constant discharging current, ΔT is the discharging time, ΔU is the potential window and m (g) is the weight of the CNFs. For the two-electrode system, the mass ratio capacitance, energy and power density of the samples were calculated as follows:

$$C = \frac{2I \times \Delta T}{m \times \Delta U}, \tag{2}$$

$$E = \frac{1}{2} C \Delta U^2, \tag{3}$$

$$P = \frac{E}{\Delta T}, \tag{4}$$

where E ($W \cdot h \cdot kg^{-1}$) is the specific energy density and P ($W \cdot kg^{-1}$) is the specific power density.

2.6 Curing kinetics of PDLF

The activation energy and reaction order are important parameters that can be calculated according to the Kissinger (Eq. (5)) and Crane (Eq. (6)) formula:

$$\ln\left(\frac{v}{T_p^2}\right) = \ln\left(\frac{AR}{E_a}\right) - \frac{E_a}{RT_p}, \tag{5}$$

$$\frac{d(\ln v)}{d\left(\frac{1}{T_p}\right)} \approx -\frac{E_a}{nR}, \tag{6}$$

where v ($°C \cdot min^{-1}$), T_p (°C), E_a ($kJ \cdot mol^{-1}$) and n are the heating rate, peak temperature, apparent activation energy, and reaction order, respectively.

3 Results and discussion

3.1 PDLF characterization

FTIR and NMR were used to analyze the functional group information of samples (Fig. 1). As shown in Fig. 1(a), the obvious absorption bands at 3359 cm^{-1} are attributed to the stretching vibrations of O–H bonds. The sharp absorbance of aromatic vibrations at 1585 cm^{-1} represents the abundance of aromatics of lignin, PDL, and PDLF resin. In addition, the saturated CH_2– stretching vibration absorption peaks are also confirmed at 2812 cm^{-1} in PDL and lignin, while the absorption peak in PDLF resins is disappeared. This indicates that the methylene produced during the phenolation process has nucleophilic addition reaction with the aldehyde group. The wavenumbers of 928 and 883 cm^{-1} are the bending vibration peaks of C–H on the furan ring structure of furfural. The absorbance at 1223 cm^{-1} belongs to the bending vibrations of ether bonds (C–O–C) in aromatic ring structure and furfural. For PDL, no peaks

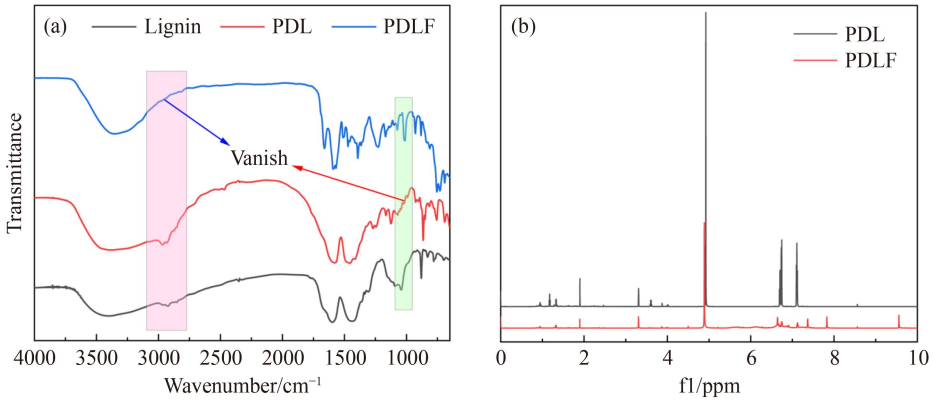

Fig. 1 FTIR spectrum of (a) lignin, PDL, and PDLF resin and (b) ^{1}H NMR spectra of PDL and PDLF resin.

are observed at 1223 cm^{-1}, which indicates that the ether bond is broken during the phenolation process. The absorption peak at 732 cm^{-1} corresponds to the substituted –CH– bending vibration peaks on the benzene ring structure. These peaks are typical characteristic peaks of phenolic resin. Consistent with the FTIR assignments, the ^{1}H NMR spectra (Fig. 1(b)) feature hydrogen shifts, as summarized in Table 1. The strong peak at 4.9 ppm was from solvent CD_4O. The aromatic peaks of both samples remained at 6.5–7.7 ppm. The aliphatic peaks of the resin samples were slightly reduced between 0.6 and 1.8 ppm, which was probably attributed to the complete involvement of PDL in the condensation reaction. Compared with PDL, the new peak at 9 ppm may be related to the introduction of phenol and aldehyde groups during the synthesis process [16].

Based on FTIR and NMR analysis and previous reports on resin [17], the reaction mechanism of DL phenolation and PDLF resin synthesis has been proposed (Scheme 1). As shown in Scheme 1(a), due to the electron-induced effect of phenolic hydroxyl groups on depolymerized lignin, nucleophilic substitution reaction can easily occur with the *o*-*p*-position of phenol, which effectively increases the active sites of phenolic hydroxyl groups in DL. Scheme 1(b) shows that the electron-rich carbons of the para-positions of phenol in PDL and the electrophilic aldehyde group in furfural can undergo nucleophilic addition. Finally, PDLF resin formed a linear and slightly branched structure.

The approximate molecular weights of PDL, PDLF, and PF resin were obtained by GPC and are presented in Fig. 2 and Table S1 (cf. Electronic Supplementary Material, ESM). Due to the hydrolysis of ether bonds and free radical cleavage of C–O or C–C bonds in the depolymerization process of lignin, its molecular weight decreased to 1002 g·mol^{-1} [18]. These small molecular structures were more beneficial for participating in the resin condensation reaction. The GPC profiles of PF and PDLF resin showed that they had similar peaks and retention times, but the molecular weights were significantly different, since PDL had a much larger molecular weight than phenol. In addition, Fig 2(b) shows that the initial temperature of thermal decomposition behavior of PF and PDLF resin was 148 and 175 °C, respectively. Thermal decomposition behavior may be caused by the alkyl chain breaking in the resin during the heating process, and part of the oligomer monomer forming gas is discharged with nitrogen [19]. At 900 °C, the remaining solid residues of PF and PDLF resin were 46.45 and 57.89 wt %, respectively. These results indicated that PDLF resin have better thermal stability and higher carbon yield because of the introduction of aromatic lignin [20].

Table 1 Band assignments for FTIR and ^{1}H NMR spectra

FTIR		^{1}H NMR		
Wavenumber/cm^{-1}	Assignment	Shift/ppm		Assignment
		PDL	PDLF	
3359	O–H stretching	1.9	1.9	OH
1661	Aromatic vibrations	3.3	3.3	CH
928	C–H vibration on the furan ring	3.6		CH_2
883		4.9	4.9	CD_4O
1223	C–O–C bending	6.7	6.6–7.8	Aromatic H
732	–CH– bending	7.1		
2812	$–CH_2–$ bending		9.6	CHO

3.2 Curing kinetics of PDLF

DSC was applied to further elaborate the curing reaction behavior of PDLF and PF resins (Fig. 3). The single peak at different heating rates in Figs. 3(a) and 3(d) indicated that the curing reaction of the materials was completed in one step [21]. When the heating rate increases, the exothermic peak shifts toward a higher temperature region. The reason is that with increasing heating rate, a large temperature difference will be generated in unit time, thereby yielding larger thermal inertia [21]. DSC scanning thermodynamic parameters of the PDLF and PF resins at different heating rates are summarized in Table S2 (cf. ESM). As shown in Fig. 3(b), according to Eq. (5), the E_a values of the PDLF and PF resins were 89.21 and 80.45 kJ·mol^{-1}, respectively. The higher molecular

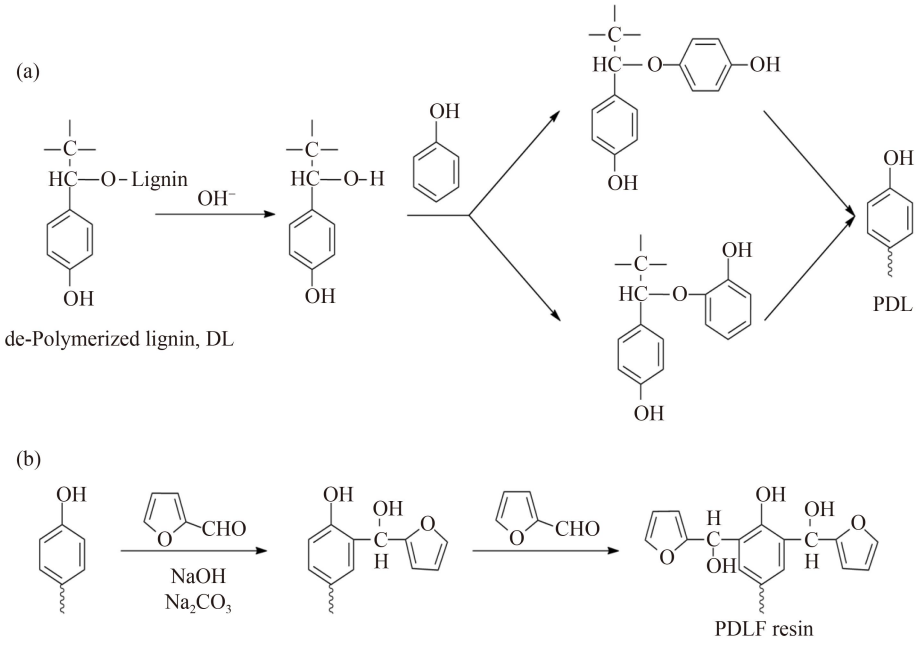

Scheme 1 (a) Reaction mechanism of PDL preparation and (b) the PDLF resin formation.

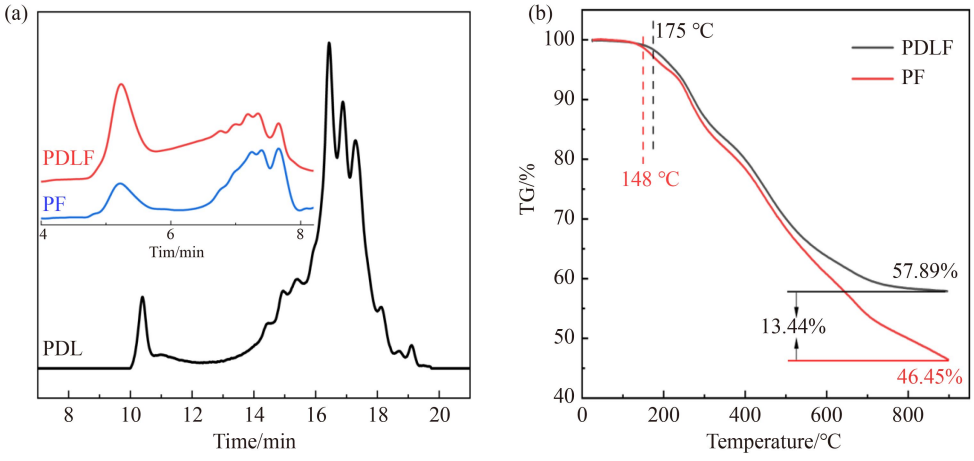

Fig. 2 (a) GPC curves of PDL, PF and PDLF resin, and (b) TG curves of PF and PDLF resin.

weight and steric hindrance of PDLF resin demand a higher activation energy than PF resin. According to Eq. (6), the reaction order of n was 0.78 and 0.72 for PDLF and PF resin, respectively (Fig. 3(e)). The fitting curves of the peak temperature and end temperature under different heating rates (Figs. 3(c) and 3(f)) for PDLF and PF resins were calculated. The results showed that the peak curing temperatures were 133 and 158 °C, while the ending temperatures were 155 and 189 °C for PDLF and PF resin, respectively. This result is mainly due to the abundant methylol groups in lignin forming methylene bridges, which promote the cross-linking curing reaction of the resin [22]. This is also consistent with previous reports that the curing temperature of phenolic resin can be effectively reduced under the action of biophenol materials [23]. For example, Cheng et al. [24] prepared bio-oil-phenol-formaldehyde resol resins with a curing temperature of 145.5 °C and Cheng et al. [16] prepared organosolv lignin phenol-formaldehyde resins with a curing temperature of 138.5 °C, both of which were lower than that of conventional PF resins (149.5 °C).

3.3 CNF and ACNF characterization

The microstructure and morphology of the fibers were examined via SEM (Fig. 4) and TEM (Fig. 5). The ACNF-PF exhibited many protrusions and droplets, as shown in Figs. 4(a, b), which caused the irregular surface of the fibers. This result may be attributed to the low molecular weight and poor spinnability of traditional PF resins. The surface of CNF-PDLF in Figs. 4(c, d) was relatively smooth, with a diameter between 400 nm and 1 μm. Upon activation, the free-standing ACNF-PDLF exhibited a uniform surface with a consistent diameter of

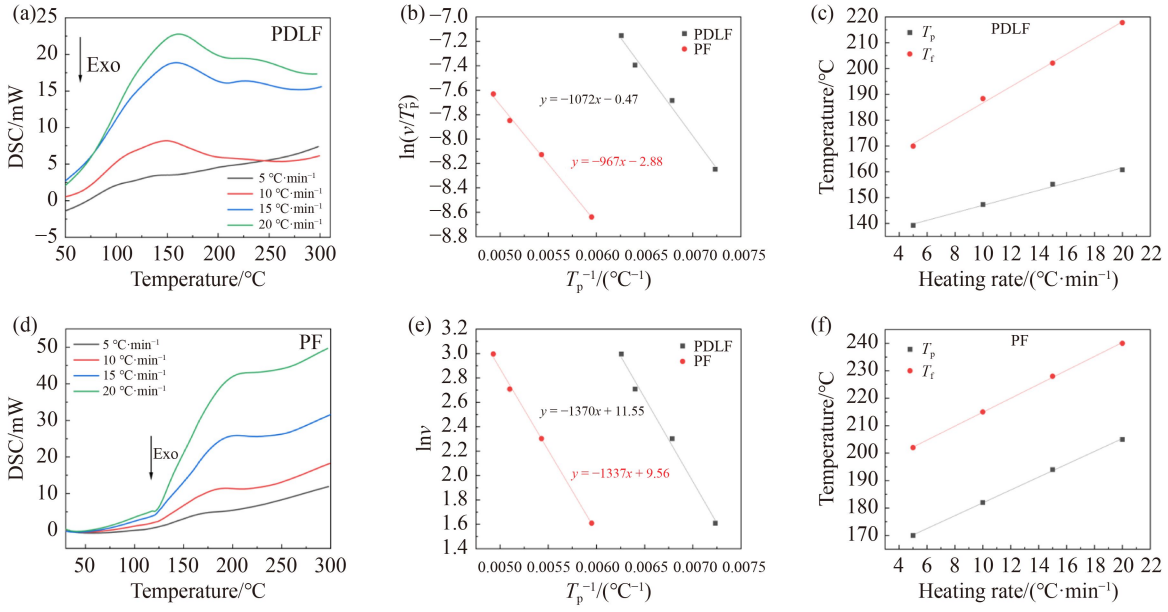

Fig. 3 DSC profile at different heating rates of (a) PDLF and (d) PF, (b) apparent activation energy and pre-finger factor fitting curve, (e) reaction series fitting curve of PDLF and PF, and curing temperature extrapolation curve of (c) PDLF and (f) PF.

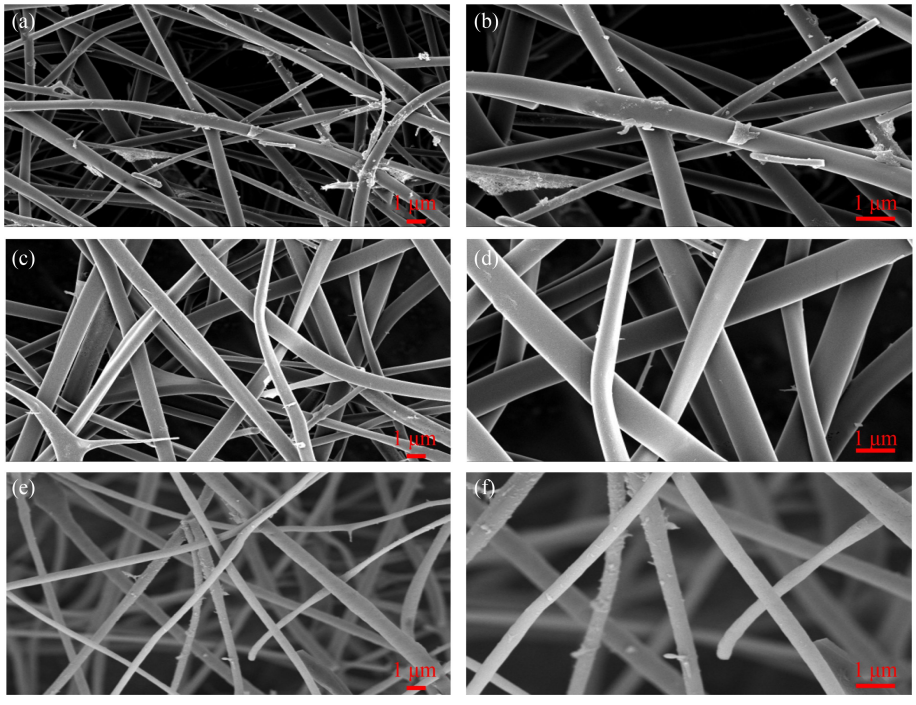

Fig. 4 SEM images of (a, b) ACNF-PF, (c, d) CNF-PDLF and (e, f) ACNF-PDLF.

approximately 400 nm. The porous structures of ACNF-PDLF were further analyzed by TEM and Brunaner–Emmett–Teller (BET) techniques.

TEM images of ACNF-PDLF in Fig. 5 show a distinctively porous structure on the surface of the carbon nanofibers. These interconnected micro/mesoporous structures were advantageous because they served as an ion buffer repository and shorten the ion diffusion pathways. Noteworthy, the yellow ring in Fig. 5(b) shows an aligned lattice stripe on the edge of the carbon fibers, which indicating that a partial graphitization region that forms in the carbon matrix can improve its electrical conductivity. The red ring exhibited a distinct interplanar spacing of 0.39 nm, which corresponded to the (002) graphitic plane.

The crystalline structure, graphitization degree, surface elements, and SSA of samples were characterized by XRD, Raman spectroscopy, XPS, and BET, respectively (Fig. 6). As exhibited in Fig. 6(a), the most relevant characteristic peaks at 23.4° and 43.4° were assigned to

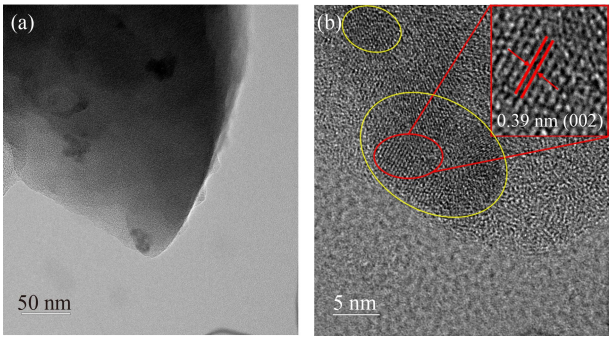

Fig. 5 TEM images of ACNF-PDLF.

the (002) and (100) planes of amorphous carbon, respectively [25]. The peaks of the samples were strong and broad in (002) and relatively weak in (100), which demonstrated that the samples possessed amorphous features with a small amount of graphite microcrystalline structure. All samples presented two distinct peaks at ~1325 and ~1590 cm^{-1} in Fig. 6(b), corresponding to D and G bands, respectively [26]. The D-band represents the disorder degree of the structure, whereas the G-band is related to the stretching vibration of carbon atoms in the sp^2 hybrid plane [27]. The I_D/I_G values of ACNF-PF, CNF-PDLF and ACNF-PDLF were calculated to be 0.91, 0.90, and 0.92, respectively. The similar I_D/I_G values

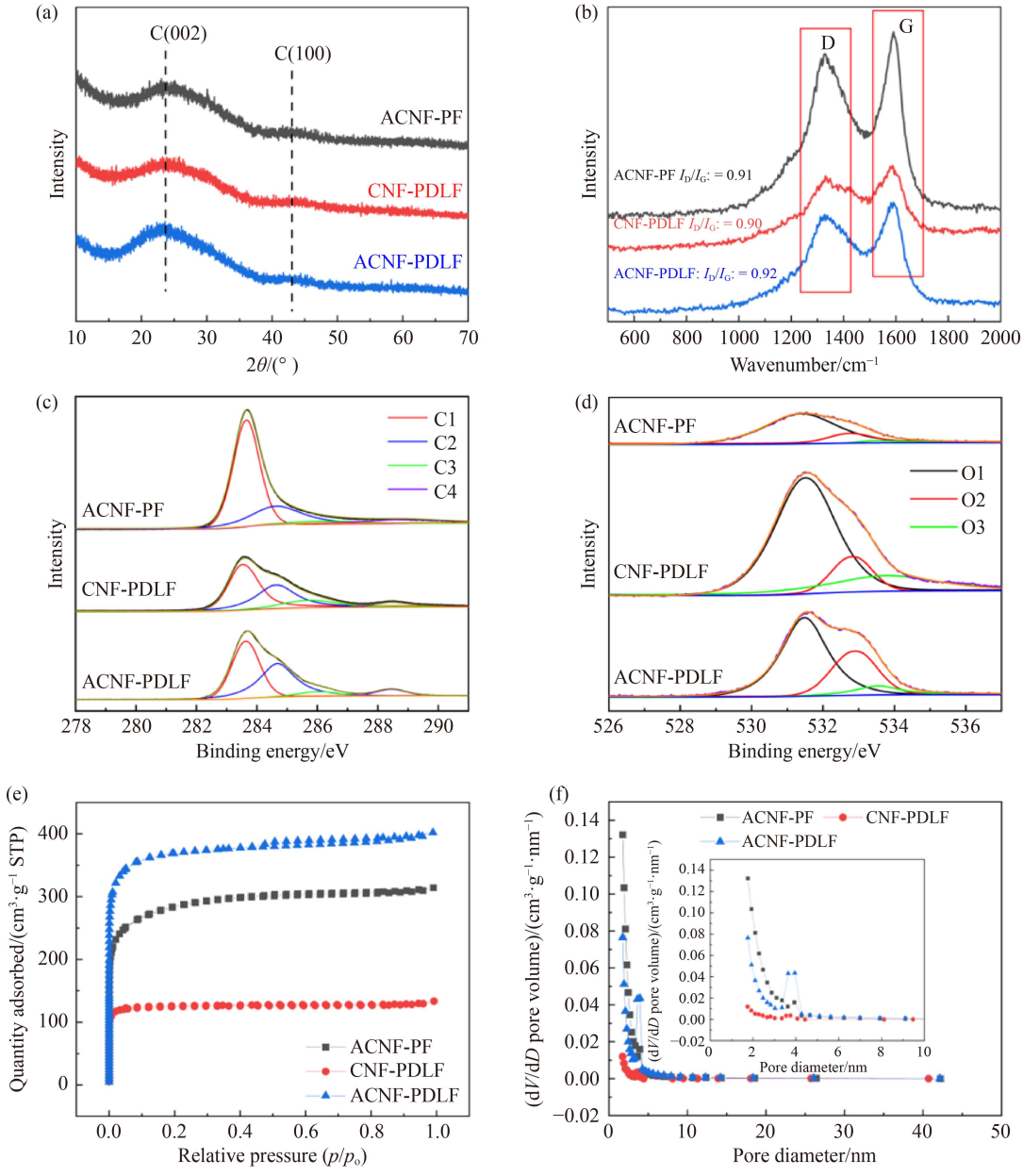

Fig. 6 (a) XRD patterns, (b) Raman spectra, XPS spectra of (c) C1s and (d) O1s, (e) nitrogen adsorption/desorption isotherms and (f) pore size distributions (BJH) of ACNF-PF, CNF-PDLF and ACNF-PDLF. The inset is a local enlargement of the pore size distributions.

showed a good graphitization degree, which ensures high electrical conductivity and subsequently effectively improves the electrochemical performance of the CNFs. The surface elemental composition of the CNFs was evaluated by XPS in Figs. 6(c, d). The XPS spectra of C1s can be deconvoluted into four peaks which corresponded to C–C (C1, 283.71 eV), C–O (C2, 284.63 eV), C=O (C3, 285.83 eV) and COO– (C4, 288.42 eV), respectively. The O1s was fitted into three peaks at 531.47, 532.84 and 533.55 eV, corresponding to C=O (O1), C–O (O2) and COO– (O3), respectively [28].

A typical type IV curve with a distinct type H_3 hysteresis loop shown in Fig. 6(e), which confirms the presence of micro/mesoporous structure [29]. The adsorption capacity was significantly enhanced at low relative pressure, especially for the ACNF-PDLF, which can be attributed to the capillary condensation resulting from abundant micropores. The detailed porosity parameters are summarized in Table 2. The ACNF-PDLF display a BET SSA of 1100 $m^2 \cdot g^{-1}$ and a total pore volume of 0.62 $cm^3 \cdot g^{-1}$, which is much higher than those of ACNF-PF (869 $m^2 \cdot g^{-1}$, 0.48 $cm^3 \cdot g^{-1}$) and CNF-PDLF (376 $m^2 \cdot g^{-1}$, 0.20 $cm^3 \cdot g^{-1}$). One can be speculated that $ZnCl_2$ acted as a Lewis to effectively remove H and O in the form of water vapor to generate pores on the surface of the fibers; in addition, the evaporation of $ZnCl_2$ in the high temperature activation process could form pores. Furthermore, KCl reacted with carbon during the activation process, resulting in a large number of porous structures in the fibers. Therefore, the SSA of CNFs was significantly increased under the action of the salt activator. The pore size distribution is exhibited in Fig. 6(f). The results showed that the ACNF-PDLF had substantial mesopores at approximately 4 nm. The mesopores can effectively improve the rate of electrolyte ion transfer and storage capacity of electrode materials.

3.4 Electrochemical performance

The electrochemical properties of CNFs and ACNF were evaluated by CV (Fig. 7). As shown in Fig. 7(a), the approximately rectangular CV curve indicates a typical electrical double-layer capacitive (EDLC) behavior [30,31]. The largest CV curve integral area of ACNF-PDLF was consistent with its highest specific capacitances compared with that of ACNF-PF and CNF-PDLF. This phenomenon is attributed to the large SSA, good electrical conductivity, and proper porosity of ACNF-PDLF, as evidenced by the BET and Raman results. These properties can synergistically and substantially accelerate ion diffusion, shorten the transport distance, and achieve high electrochemical performance. Figures 7(b–d) show the CV curves of the CNFs and ACNF samples at 5–100 $mV \cdot s^{-1}$. The CV curve without an obvious change in shape at 100 $mV \cdot s^{-1}$, indicates an excellent capacitor response and rate capability [32].

To further verify the influence of the SSA and pore structure on the electrochemical performance, the rate performance and cycling stability of CNFs and ACNF electrodes were evaluated (Fig. 8). The GCD of all specimens showed triangular shapes with good symmetry in Fig. 8(a), which represents the EDLC behavior and excellent electrochemical reversibility [33,34], and is consistent with the CV measurement. As shown in Fig. 8(b) and Table S3 (cf. ESM), ACNF-PDLF possessed a specific capacitance of 238 $F \cdot g^{-1}$ at 0.1 $A \cdot g^{-1}$, which was superior to ACNF-PF (185 $F \cdot g^{-1}$) and CNF-PDLF (222 $F \cdot g^{-1}$), demonstrated that the porous ACNF-PDLF facilitated the ion transport of the electrolyte and reduced the ion diffusion lengths. The discharge time was higher than charging time (e.g., 2270 versus 1372 s for ACNF-PDLF), indicating excellent coulombic efficiency. The gravimetric capacitance (C/($F \cdot g^{-1}$)) values of ACNF-PF, CNF-PDLF, and ACNF-PDLF at various current densities (0.1 to 20 $A \cdot g^{-1}$) were calculated according to Eq. (1) as illustrated in Fig. 8(b). ACNF-PDLF exhibited excellent specific capacitances of 238 and 168 $F \cdot g^{-1}$ at 0.1 and 20 $A \cdot g^{-1}$, respectively, with a capacitance retentions of 71%. Furthermore, when the current density gradually increased from 0.1 to 20 $A \cdot g^{-1}$, the corresponding C values of ACNF-PF and CNF-PDLF decreased to 147 $F \cdot g^{-1}$ with capacitance retentions of 80 (80%) and 66%, respectively. Compared to ACNF-PF and CNF-PDLF, ACNF-PDLF consistently exhibited the highest value of C at various current densities. This may be speculated that the large SSA and proper porosity of ACNF-PDLF favors the diffusion of electrolyte ions to the active sites of the surface by reducing the transfer distance. As shown in Fig. S1 (cf. ESM), the quasi-triangular structure presented good symmetry even at a high current density of 20 $A \cdot g^{-1}$, indicating excellent rate performance. These results correspond to the CV curves in Figs. 7(b–d) and reflect the good rate performance and stability of the carbon fibers. Furthermore, cycle life tests

Table 2 Porosity and electrochemical properties of the samples

Sample	S_{BET}[a)]/($m^2 \cdot g^{-1}$)	S_{Mic}[b)]/($m^2 \cdot g^{-1}$)	V_{total}[c)]/($cm^3 \cdot g^{-1}$)	V_{Mic}/($cm^3 \cdot g^{-1}$)	Pore size[d)]/nm	C_{KOH}[e)]/($F \cdot g^{-1}$)
ACNF-PF	869	551	0.48	0.29	2.6	155
CNF-PDLF	376	345	0.20	0.18	4.3	165
ACNF-PDLF	1100	902	0.62	0.48	3.2	208

a) Specific surface area calculated by BET equation; b) specific surface area of micropores calculated by t-plot method; c) total pore volume was obtained by N_2 adsorption isotherm at $p/p_0 = 0.995$; d) pore size distribution was calculated from N_2 adsorption isotherm by BJH theory; e) specific capacitance obtained at current density of 1 $A \cdot g^{-1}$ in 6 $mol \cdot L^{-1}$ KOH.

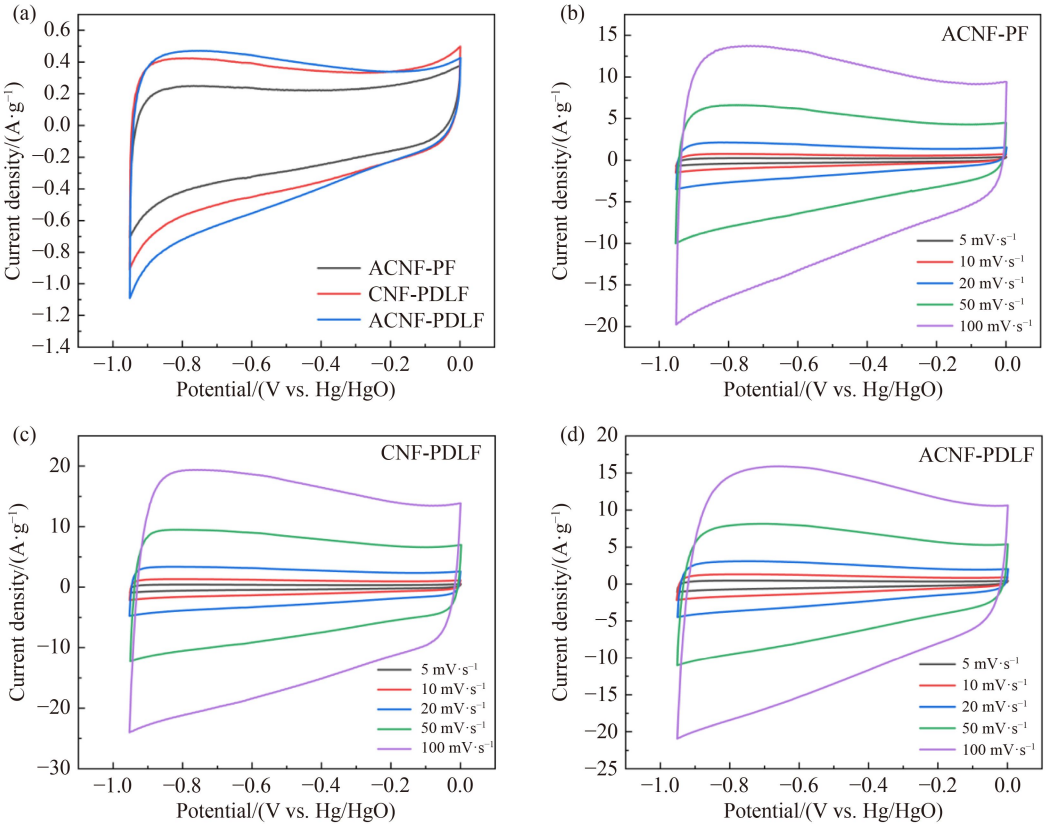

Fig. 7 (a) The CV curve of ACNF-PF, CNF-PDLF and ACNF-PDLF at scan rates of 5 mV·s^{-1}. (b) Cyclic voltammograms of ACNF-PF, (c) CNF-PDLF and (d) ACNF-PDLF electrode materials at scan rates of 5, 10, 20, 50, and 100 mV·s^{-1}.

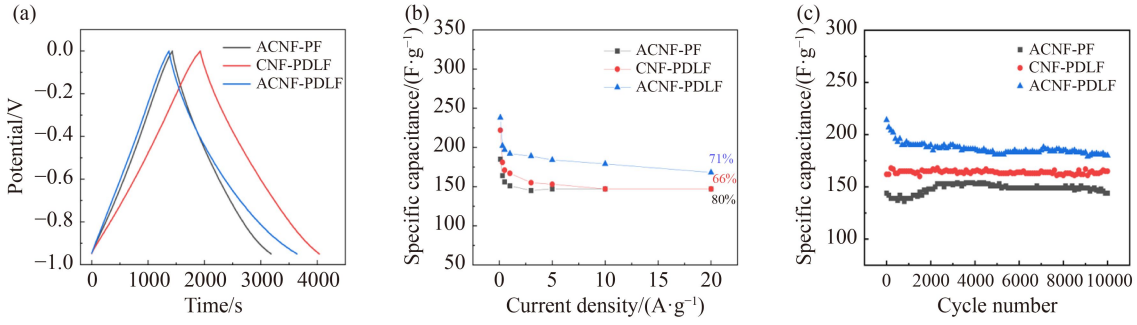

Fig. 8 (a) GCD curves at current density of 0.1 A·g^{-1}, (b) rate performance, (c) cyclic performance curve of ACNF-PF, CNF-PDLF and ACNF-PDLF.

were conducted at 1 A·g^{-1} (Fig. 8(c)). For ACNF-PDLF electrodes, the initial specific capacitance retained 84% after 10000 cycles while the capacitance retentions of ACNF-PF and CNF-PDLF was 94% and 98%, respectively. The high capacity retention rate indicates the excellent stability of the free-standing fiber samples.

The diffusion resistance and charge transfer resistance of CNFs and ACNF were related to the characteristics of EIS curves in Fig. 9. All samples in the low-frequency region showed good linear shapes (Fig. 9(a)), which represent the typical EDLC behavior. The R_s values for ACNF-PF, CNF-PDLF, and ACNF-PDLF were 0.42, 0.43, and 0.53 Ω, respectively, from the EIS fitting curve (Fig. S2 (cf. ESM), EIS data were fitted using Zview2 software). The lower R_s was attributed to the binder-free and free-standing nature of CNFs (see Fig. 9(b)). Apparently, the ACNF-PDLF possessed the smaller diameter of semicircle, the shortest length and the steepest slope of the curves, suggesting the lowest charge transfer resistance, diffusion resistivity, and high capacitance [35,36]. Thus, ACNF-PDLF had the largest specific capacitance, which corresponded to the results of GCD and CV. In addition, the conductivity test results of fiber samples demonstrated that ACNF-PDLF had better conductivity (0.38 S·cm^{-1}) than ACNF-PF (0.24 S·cm^{-1}) and CNF-PDLF (0.29 S·cm^{-1}). With low resistance and high conductivity, ACNF-PDLF was conducive to the rapid transmission of electrons and achieved a large specific capacitances.

To further investigate the electrochemical cell perfor-

mance (Fig. S3, cf. ESM), symmetric supercapacitors (SSCs) were assembled using two identical carbon fibers electrodes. To verify the durability and cycle stability of the carbon fibers electrodes, GCD tests were performed for up to 10000 cycles at 1 $A \cdot g^{-1}$ (Fig. S3(a)). ACNF-PDLF possessed a specific capacitances of 144 $F \cdot g^{-1}$ at 1 $A \cdot g^{-1}$, which was superior to ACNF-PF (90 $F \cdot g^{-1}$) and CNF-PDLF (110 $F \cdot g^{-1}$). The results elucidate that ACNF-PDLF has a large SSA and rich porosity, which improved the surface accessibility and speed up electrolyte ion transfer in the process of double electrical layer energy storage. All samples had remarkable cycling stability after 10000 cycles.

The electrochemical performance of SSCs at different current densities was studied, as shown in Fig. S3(b). ACNF-PDLF exhibited excellent specific capacitances of 190 and 100 $F \cdot g^{-1}$ at 0.1 and 5 $A \cdot g^{-1}$, respectively. The ACNF-PF and CNF-PDLF electrodes exhibited specific capacitances of 106 and 150 $F \cdot g^{-1}$ at 0.1 $A \cdot g^{-1}$, respectively. With gradually increasing the current density from 0.1 to 5 $A \cdot g^{-1}$, the corresponding C values of ACNF-PF and CNF-PDLF decreased to 65 and 95 $F \cdot g^{-1}$ with capacitance retentions of 61 (61%) and 63%, respectively. The specific capacitances of the carbon fibers decreased with increasing current density, mainly due to the fact that the electrolyte ions cannot reach the electrode surface in a limited time to form a double layer. Therefore, the specific capacitance was lower at a high current density.

The energy density and power density (as shown in Fig. 10 and Table S3 (cf. ESM)) of SSC were calculated by using Eqs. (3) and (4) [37,38]. The ACNF-PDLF SSC could supply a maximal energy density of 26.39 $W \cdot h \cdot kg^{-1}$ where the power density was 100 $W \cdot kg^{-1}$, which was superior to that of ACNF-PF (14.72 $W \cdot h \cdot kg^{-1}$) and CNF-PDLF (20.83 $W \cdot h \cdot kg^{-1}$). ACNF-PDLF SSC performed better than the recently reported biomass-based electrode materials, such as N, S co-doped porous carbon nanosheets derived from willow catkin [39], cellulose acetate carbon nanofibers [40], hierarchical porous carbons derived from corn straw [41], and halloysite nanotube/carbon [32]. The energy density of the three samples remained above 9.03 $W \cdot h \cdot kg^{-1}$ even at a high power density of 5 $kW \cdot kg^{-1}$. The electrochemical performance of carbon nanofibers prepared from different materials as electrode materials of supercapacitors is shown in Table 3. Compared with the literature, ACNF-PDLF has a higher specific capacitance and a longer cycle life. Its excellent electrochemical properties were due to the combined effect of the high SSA, suitable pore structure, and low resistance. Thus, the free-standing ACNF-PDLF is expected to be widely used as an effective energy storage material for supercapacitors.

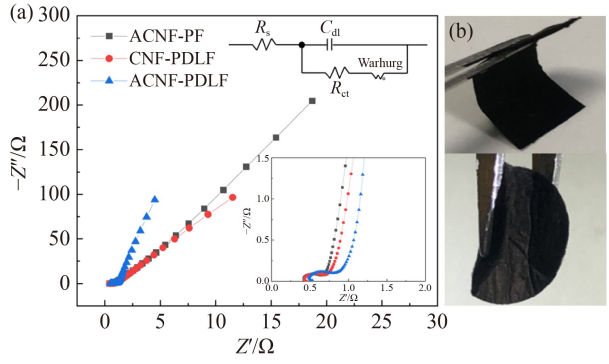

Fig. 9 (a) Nyquist impedance plot of ACNF-PF, CNF-PDLF and ACNF-PDLF. The insets are the equivalent electrical circuit diagram and enlarged high-frequency region of the plots. (b) The binder-free ACNF-PDLF electrode has good self-supporting characteristics.

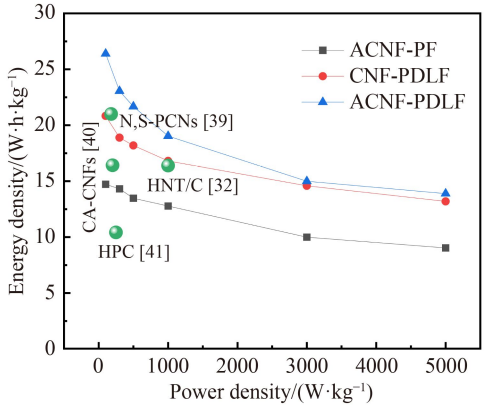

Fig. 10 The Ragone plots of the symmetric cell and comparative performance of the symmetric cell versus previously reported ones (Refs.: N,S-PCNs [39], CA-CNFs [40], HPC [41], HNT/C [32]).

Table 3 Electrochemical performance for carbon nanofibers reported in the literature.

Materials	Electrolyte	Current density or scan rates	$C/(F \cdot g^{-1})$	Cyclic stability	Ref.
Phenolic-based carbon nanofiber webs	6 $mol \cdot L^{-1}$ KOH	0.1 $A \cdot g^{-1}$	157	–	[8]
PAN/PMMA-derived carbon nanofibers	2 $mol \cdot L^{-1}$ KOH	2 $mV \cdot s^{-1}$	210	2000/100%	[42]
Porous carbon nanofibers	0.5 $mol \cdot L^{-1}$ H_2SO_4	0.2 $A \cdot g^{-1}$	104.5	2000/94%	[43]
Carbon nanofiber/graphene	6 $mol \cdot L^{-1}$ KOH	1 $A \cdot g^{-1}$	183	4500/92%	[44]
Nitrogen-doped porous carbon nanofibers	6 $mol \cdot L^{-1}$ KOH	0.1 $A \cdot g^{-1}$	202	3000/97%	[45]
Porous carbon nanofiber webs	6 $mol \cdot L^{-1}$ KOH	10 $mV \cdot s^{-1}$	140	/	[46]
ACNF-PDLF	6 $mol \cdot L^{-1}$ KOH	0.1 $A \cdot g^{-1}$	238	10000/84%	This work
			190	10000/98% (SSCs)	

4 Conclusions

The present work provides a feasible approach to prepare free-standing activated carbon nanofibers with binder-free and high specific surface areas from PDLF resins. The ACNF-PDLF obtained by salt activation has an interconnected pore structure, which is composed of abundant mesopores and micropores, showing exceptional electrochemical performance. The ACNF-PDLF exhibits a remarkable specific capacitance of 238 $F \cdot g^{-1}$ at 0.1 $A \cdot g^{-1}$, as well as significant rate performance and cyclic stability. The ACNF-PDLF based symmetric supercapacitor, prepared with a two-electrode configuration, exhibits an energy density of 26.39 $W \cdot h \cdot kg^{-1}$, whereas the power density was 100 $W \cdot kg^{-1}$. Furthermore, it shows an outstanding capacitance retention of 98% even after 10000 charge–discharge cycles. These results might provide a route for preparing bio-based carbon fibers with a high specific surface area and appropriate pore structure from PDLF resins for high-performance supercapacitors.

Acknowledgements This work was supported by the National Natural Science Foundation of China (Grant Nos. 21908204, 52074244) and the Henan Provincial Key Research and Development Program (Grant No. 192102310202). The authors would also like to acknowledge the support from Zhengzhou University.

Electronic Supplementary Material Supplementary material is available in the online version of this article at https://dx.doi.org/10.1007/s11705-022-2260-1 and is accessible for authorized users.

References

1. Li Z, Gadipelli S, Yang Y, He G, Guo J, Li J, Lu Y, Howard C A, Brett D J L, Parkin I P, Li F, Guo Z. Exceptional supercapacitor performance from optimized oxidation of graphene-oxide. Energy Storage Materials, 2019, 17: 12–21
2. Li Y, Huang J, Kang L, Tian Z, Lai F, Brett D J L, Liu T, He G. Self-assembled carbon nanoribbons with the heteroatom doping used as ultrafast charging cathodes in zinc-ion hybrid supercapacitors. Science China Materials, 2022, 65(6): 1495–1502
3. Sui D, Chang M, Wang H, Qian H, Yang Y, Li S, Zhang Y, Song Y. A brief review of catalytic cathode materials for Na-CO_2 batteries. Catalysts, 2021, 11(5): 603–605
4. Zhang W, Yuan X, Yan X, You M, Jiang H, Miao J, Zhou W, Zhu Y, Cheng X. Tripotassium citrate monohydrate derived carbon nanosheets as a competent assistant to manganese dioxide with remarkable performance in the supercapacitor. Frontiers of Chemical Science and Engineering, 2022, 16(3): 420–432
5. Lei C, Amini N, Markoulidis F, Wilson P, Tennison S, Lekakou C. Activated carbon from phenolic resin with controlled mesoporosity for an electric double-layer capacitor (EDLC). Journal of Materials Chemistry A: Materials for Energy and Sustainability, 2013, 1(19): 6037–6042
6. Ji H K, Ko Y I, Kim Y A, Kim K S, Yang C M. Sulfur-doped carbon nanotubes as a conducting agent in supercapacitor electrodes. Journal of Alloys and Compounds, 2021, 855: 157282
7. Li Z F, Zhang H, Liu Q, Sun L, Xie J. Fabrication of high-surface-area graphene/polyaniline nanocomposites and their application in supercapacitors. ACS Applied Materials & Interfaces, 2013, 5(7): 2685–2691
8. Ma C, Song Y, Shi J, Zhang D, Zhong M, Guo Q, Liu L. Phenolic-based carbon nanofiber webs prepared by electrospinning for supercapacitors. Materials Letters, 2012, 76: 211–214
9. Jain A, Tripathi S K. Fabrication and characterization of energy storing supercapacitor devices using coconut shell based activated charcoal electrode. Materials Science and Engineering B, 2014, 183: 54–60
10. Zheng Z, Gao Q. Hierarchical porous carbons prepared by an easy one-step carbonization and activation of phenol–formaldehyde resins with high performance for supercapacitors. Journal of Power Sources, 2011, 196(3): 1615–1619
11. Du B, Zhu H, Chai L, Cheng J, Wang X, Chen X, Zhou J, Sun R. Effect of lignin structure in different biomass resources on the performance of lignin-based carbon nanofibers as supercapacitor electrode. Industrial Crops and Products, 2021, 170: 113745
12. Chen W, Wang H, Lan W, Li D, Zhang A, Liu C. Construction of sugarcane bagasse-derived porous and flexible carbon nanofibers by electrospinning for supercapacitors. Industrial Crops and Products, 2021, 170: 113700
13. Si L, Yan K, Li C, Huang Y, Pang X, Yang X, Sui D, Zhang Y, Wang J, Charles Xu C. Binder-free SiO_2 nanotubes/carbon nanofibers mat as superior anode for lithium-ion batteries. Electrochimica Acta, 2022, 404: 139747
14. Zhang Y, Ferdosian F, Yuan Z, Xu C. Sustainable glucose-based phenolic resin and its curing with a DGEBA epoxy resin. Journal of the Taiwan Institute of Chemical Engineers, 2017, 71: 381–387
15. Xi Y, Yang D, Qiu X, Wang H, Huang J, Li Q. Renewable lignin-based carbon with a remarkable electrochemical performance from potassium compound activation. Industrial Crops and Products, 2018, 124: 747–754
16. Cheng S, Yuan Z, Leitch M, Anderson M, Xu C. Highly efficient de-polymerization of organosolv lignin using a catalytic hydrothermal process and production of phenolic resins/adhesives with the depolymerized lignin as a substitute for phenol at a high substitution ratio. Industrial Crops and Products, 2013, 44: 315–322
17. Mahmood N, Xu C, Zhang Y, Huang S, Yuan Z. Sustainable bio-phenol-hydroxymethylfurfural resins using phenolated de-polymerized hydrolysis lignin and their application in bio-composites. Industrial Crops and Products, 2016, 79: 84–90
18. Minami E, Kawamoto H, Saka S. Reaction behavior of lignin in supercritical methanol as studied with lignin model compounds. Journal of Wood Science, 2003, 49(2): 158–165
19. Lee Y K, Kim D J, Kim H J, Hwang T S, Sokolov J. Activation energy and curing behavior of resol- and novolac-type phenolic resins by differential scanning calorimetry and thermogravimetric analysis. Journal of Applied Polymer Science, 2010, 89(10):

2589–2596

20. Zhang Y, Yuan Z, Xu C. Engineering biomass into formaldehyde-free phenolic resin for composite materials. AIChE Journal, 2015, 61(4): 1275–1283
21. Xu W B, Bao S P, Shen S J, Hang G P, He P S. Curing kinetics of epoxy resin-imidazole-organic montmorillonite nanocomposites determined by differential scanning calorimetry. Journal of Applied Polymer Science, 2010, 88(13): 2932–2941
22. Wang M, Leitch C. Synthesis of phenol-formaldehyde resol resins using organosolv pine lignins. European Polymer Journal, 2009, 45(12): 3380–3388
23. Khan M A, Ashraf S M, Malhotra V P. Eucalyptus bark lignin substituted phenol formaldehyde adhesives: a study on optimization of reaction parameters and characterization. Journal of Applied Polymer Science, 2004, 92(6): 3514–3523
24. Cheng S, D'Cruz I, Yuan Z, Wang M, Anderson M, Leitch M, Xu C C. D"Cruz I, Yuan Z, Wang M, Anderson M, Leitch M, Xu C. Use of biocrude derived from woody biomass to substitute phenol at a high-substitution level for the production of biobased phenolic resol resins. Journal of Applied Polymer Science, 2011, 121(5): 2743–2751
25. Zhuang Q Q, Cao J P, Zhao X Y, Wu Y, Wei X Y. Preparation of layered-porous carbon from coal tar pitch narrow fractions by single-solvent extraction for superior cycling stability electric double layer capacitor application. Journal of Colloid and Interface Science, 2020, 567: 347–356
26. Sui D, Xu L, Zhang H, Sun Z, Kan B, Ma Y, Chen Y. A 3D cross-linked graphene-based honeycomb carbon composite withexcellent confinement effect of organic cathode material for lithium-ion batteries. Carbon, 2020, 157: 656–662
27. Sui D, Wu M, Shi K, Li C, Lang J, Yang Y, Zhang X, Yan X, Chen Y. Recent progress of cathode materials for aqueous zinc-ion capacitors: carbon-based materials and beyond. Carbon, 2021, 185: 126–151
28. Wu F, Gao J, Zhai X, Xie M, Sun Y, Kang H, Tian Q, Qiu H. Hierarchical porous carbon microrods derived from albizia flowers for high performance supercapacitors. Carbon, 2019, 147: 242–251
29. Wu Y, Cao J P, Zhao X Y, Hao Z Q, Zhuang Q Q, Zhu J S, Wang X Y, Wei X Y. Preparation of porous carbons by hydrothermal carbonization and KOH activation of lignite and their performance for electric double layer capacitor. Electrochimica Acta, 2017, 252: 397–407
30. Dandan G, Jin Q, Ranran X, Zhen Z, Wei J. Facile synthesis of nitrogen-enriched nanoporous carbon materials for high performance supercapacitors. Journal of Colloid and Interface Science, 2019, 538: 199–208
31. Wang J G, Yang Y, Huang Z H, Kang F. A high-performance asymmetric supercapacitor based on carbon and carbon-MnO_2 nanofiber electrodes. Carbon, 2013, 61: 190–199
32. Yang X, Zeng X, Han G, Sui D, Zhang Y. Preparation and performance of porous carbon nanocomposite from renewable phenolic resin and halloysite nanotube. Nanomaterials, 2020, 10(9): 1703
33. Hao Z Q, Cao J, Dang Y L, Wu Y, Zhao X Y, Wei X Y. Three-dimensional hierarchical porous carbon with high oxygen content derived from organic waste liquid with superior electric double layer performance. ACS Sustainable Chemistry & Engineering, 2019, 7(4): 4037–4046
34. Guan T, Li K, Zhao J, Zhao R, Zhang G, Zhang D, Wang J. Template-free preparation of layer-stacked hierarchical porous carbons from coal tar pitch for high performance all-solid-state supercapacitors. Journal of Materials Chemistry A: Materials for Energy and Sustainability, 2017, 5(30): 15869–15878
35. He X, Zhao N, Qiu J, Xiao N, Yu M, Yu C, Zhang X, Zheng M. Synthesis of hierarchical porous carbons for supercapacitors from coal tar pitch with nano-Fe_2O_3 as template and activation agent coupled with KOH activation. Journal of Materials Chemistry A: Materials for Energy and Sustainability, 2013, 1(33): 9440–9448
36. Wang W, Lv H, Du J, Chen A. Fabrication of N-doped carbon nanobelts from a polypyrrole tube by confined pyrolysis for supercapacitors. Frontiers of Chemical Science and Engineering, 2021, 15(5): 1312–1321
37. Zhang D, He C, Wang Y, Zhao J, Wang J, Li K. Oxygen-rich hierarchically porous carbons derived from pitch-based oxidized spheres for boosting the supercapacitive performance. Journal of Colloid and Interface Science, 2019, 540: 439–447
38. Yan J, Liu J, Fan Z, Wei T, Zhang L. High-performance supercapacitor electrodes based on highly corrugated graphene sheets. Carbon, 2012, 50(6): 2179–2188
39. Li Y, Wang G, Wei T, Fan Z, Yan P. Nitrogen and sulfur co-doped porous carbon nanosheets derived from willow catkin for supercapacitors. Nano Energy, 2016, 19: 165–175
40. Wang Y, Cui J, Qu Q, Ma W, Li F, Du W, Liu K, Zhang Q, He S, Huang C. Free-standing porous carbon nanofiber membranes obtained by one-step carbonization and activation for high-performance supercapacitors. Microporous and Mesoporous Materials, 2022, 329: 111545
41. Ma H, Chen Z, Wang X, Liu Z, Liu X. A simple route for hierarchically porous carbon derived from corn straw for supercapacitor application. Journal of Renewable and Sustainable Energy, 2019, 11(2): 024102
42. Lai C C, Lo C T. Preparation of nanostructural carbon nanofibers and their electrochemical performance for supercapacitors. Electrochimica Acta, 2015, 183: 85–93
43. Liu Y, Zhou J, Lu C. Highly flexible freestanding porous carbon nanofibers for electrodes materials of high-performance all-carbon supercapacitors. ACS Applied Materials & Interfaces, 2015, 7(42): 23515–23520
44. Dong Q, Wang G, Hu H, Yang J, Qian B, Ling Z, Qiu J. Ultrasound-assisted preparation of electrospun carbon nanofiber/graphene composite electrode for supercapacitors. Journal of Power Sources, 2013, 243: 350–353
45. Chen L F, Zhang X D, Liang H W, Kong M, Guan Q F, Chen P, Wu Z Y, Yu S H. Synthesis of nitrogen-doped porous carbon nanofibers as an efficient electrode material for supercapacitors. ACS Nano, 2012, 6(8): 7092–7102
46. Kim C, Btn N, Yang K S, Kojima M, Kim Y A, Kim Y J, Endo M, Yang S C. Self-sustained thin webs consisting of porous carbon nanofibers for supercapacitors via the electrospinning of polyacrylonitrile solutions containing zinc chloride. Advanced Materials, 2010, 19(17): 2341–2346